Nano Research
2023, 16(1): 239–247

ISSN 1998-0124 CN 11-5974/O4
https://doi.org/10.1007/s12274-022-4712-9

Research Article

Hot spots engineering by dielectric support for enhanced photocatalytic redox reactions

Yan Yu[1,2], Yujun Xie[2], Pengfei Zhang[1], Wei Zhang[1,3], Wenxing Wang[1] (✉), Shuyu Zhang[2] (✉), Qiongrong Ou[2], and Wei Li[1] (✉)

[1] *Department of Chemistry, State Key Laboratory of Molecular Engineering of Polymers, Shanghai Key Lab of Molecular Catalysis and Innovative Materials, Laboratory of Advanced Materials, Fudan University, Shanghai 200433, China*
[2] *Institute for Electric Light Sources, School of Information Science and Technology, Fudan University, Shanghai 200433, China*
[3] *Zhuhai Fudan Innovation Institute, Guangdong-Macao In-Depth Cooperation Zone in Hengqin, Zhuhai 519000, China*

Received: 1 June 2022 / **Revised:** 26 June 2022 / **Accepted:** 27 June 2022

ABSTRACT

Regulating the surface plasmon resonance (SPR) of metallic nanostructures is of great interests for optical and catalytic applications, however, it is still a great challenge for tuning SPR features of small metallic nanoparticles (< 10 nm). In this work, we design a unique dielectric support—urchin-like mesoporous silica nanoparticles (U-SiO_2) with ordered long spikes on its surface, which can well enhance the SPR properties of ~ 3 nm gold nanocrystals (AuNCs). The U-SiO_2 not only realizes the uniform self-assembly of AuNCs, but also prevents their aggregation due to the unique confinement effect. The finite-difference time-domain simulations show that the AuNCs on U-SiO_2 can generate plasmonic hot spots with highly enhanced electromagnetic field. Moreover, the hot electrons can be effectively and rapidly transferred through the interface junction to TiO_2. Thus, a high visible-light-driven photocatalytic activity can be observed, which is 3.8 times higher than that of smooth photocatalysts. The concept of dielectric supports engineering provides a new strategy for tuning SPR of small metallic nanocrystals towards the development of advanced plasmon-based applications.

KEYWORDS

surface plasmon resonance, hot spots, urchin-like silica nanoparticles, photocatalysis, core–shell structures, TiO_2

1 Introduction

Surface plasmon resonance (SPR) refers to a resonant oscillation of free electrons close to the surface of metal coupled by light [1–4]. Through the excitation of SPR, plasmonic metallic nanostructures exhibit the unprecedented capacity to concentrate electromagnetic fields, scatter electromagnetic radiation, and convert the energy of photons into heat [5–8]. These unique properties have propelled them in a wide range of applications, including molecular sensing [9, 10], surface-enhanced Raman scattering spectroscopy [11, 12], plasmonic waveguides [13, 14], thermal emitters [15, 16], photocatalysis [17, 18] and solar cells [19, 20]. In this case, it is of great significance to tune the wavelength and intensity of SPR. To date, various methods have been developed to control the compositions, sizes, and shapes of individual plasmon nanoparticles (e.g., gold nanorods [17], gold nanostars [21], and AuPd nanowheels [22]) and assemble the plasmonic nanoparticles into closely interacted architectures (e.g., nanochains [23, 24] and nanocatalosomes [25]) towards extending the wavelength and enhancing the intensity of SPR effect.

Small metal nanoparticles can facilitate the formation of metal/semiconductor Schottky junction, thus realizing the fast electron transfer through the interface for efficient photocatalysis [26–30]. However, the application of small-sized metal nanoparticles to enhance the light absorption in visible light region of semiconductors is rarely reported. This is because that, unlike large nanoparticles (> 10 nm), the SPR band is strongly damped and even no longer supported for metallic nanocrystals with small sizes (for Au, < 2 nm) [31–33]. Notably, it is interesting that the SPR of small metallic nanocrystals can also be effectively tailored by the dielectric environment [34]. Attempts have been made to tune the SPR of plasmon metallic nanostructures by introducing a dielectric support to adjust the near field scattering of the plasmon metallic nanostructures [28, 29, 35]. However, to date, the metallic nanocrystals are sparsely distributed on the dielectric supports. In such circumstances, the SPR aroused from isolated small nanocrystals is inherently weak and the distance between the adjacent nanocrystals is too large to excite the plasmonic coupling effect [1, 11], making it difficult to produce distinct SPR effect. Another key problem is that the metallic nanocrystals are generally at a thermodynamic unstable state and easily suffer from severe aggregation in the subsequent application processing due to their small particle size and high surface energy [28, 36, 37].

In this work, we report a dielectric support engineering strategy to enhance the SPR effect of sub-5 nm gold nanocrystals (AuNCs) by preparing urchin-like mesoporous silica support with ordered long spikes as a novel support. The urchin-like silica nanosupport

Address correspondence to Wenxing Wang, wangwenxing@fudan.edu.cn; Shuyu Zhang, zhangshuyu@fudan.edu.cn; Wei Li, weilichem@fudan.edu.cn

not only has a high specific surface area, which can provide abundant binding sites to realize tight assembly of AuNCs for exciting the plasmon-coupling effect, but also confines the AuNCs in spikes matrix with high stability. Moreover, the urchin-like silica nanosupport facilitates the uniform coating of TiO_2 and prevents the aggregation of AuNCs during the crystallization and subsequent catalytic processes. In consequence, the sufficient contact between AuNCs and TiO_2 enables the formation of abundant interfaces for efficient electron transfer. The finite-difference time-domain (FDTD) simulations demonstrate that the plasmonic resonances of adjacent AuNCs assembled on urchin-like nanosupport are strongly coupled, giving rise to plasmon hot spots with highly intense and localized electric field. The ultraviolet–visible (UV–Vis) diffuse reflectance spectrum (DRS) and photoelectrochemical experiment results show that the urchin-like photocatalysts possess enhanced light absorption and higher photocurrent density under visible light illumination. For photodegradation of tetracycline hydrochloride (TCH) under visible light illumination, the crystalline urchin-like photocatalysts realized 52.91% degradation after 30 min irradiation, achieving a 2.9-fold improvement compared to the photocatalyst supported by conventional silica nanospheres. Besides, the crystalline urchin-like photocatalysts obtained H_2 generation rate of 318.35 $\mu mol \cdot h^{-1} \cdot g^{-1}$ under solar light, which is 3.8 times higher than that of the conventional silica nanospheres-supported photocatalysts.

2 Experimental

2.1 Chemicals and materials

All chemicals were purchased from commercial suppliers and used without further purification. Cetyltrimethyl ammonium bromide (CTAB, > 98.0%) and tetrakishydroxymethyl-phosphonium chloride (THPC, 80% in H_2O) were purchased from Sigma-Aldrich (Shanghai, China). Gold chloride trihydrate ($HAuCl_4 \cdot 3H_2O$, ≥ 99.9%), TCH (UPS), ammonium hydroxide solution ($NH_3 \cdot H_2O$), tetraethyl orthosilicate (TEOS), (3-aminopropyl) triethoxysilane (APTES, 98%), sodium hydroxide (NaOH, ≥ 98%), cyclohexane (≥ 99.9%), titanium(IV) isopropoxide (TIP, 99.9%), 1-hexadecylamine (HDA, 98%), and methanol (≥ 99.9%) were purchased from Aladdin.

2.2 Synthesis of positively charged silica nanoparticles (U-SiO_2-20, U-SiO_2-10, and S-SiO_2)

The urchin-like mesoporous silica nanoparticles (U-SiO_2) with surfaces rich of longer spikes and shorter spikes were synthesized via an epitaxial growth approach [38]. Briefly, 20 mL TEOS in cyclohexane (20 vol.%) was added to 50 mL aqueous solution containing 1 g CTAB and 0.8 mL NaOH (0.1 M). The mixture was stirred at 60 °C for reaction. The reaction time was 72 h for U-SiO_2-20 and 48 h for U-SiO_2-10. After reaction, the obtained solution containing U-SiO_2-20 or U-SiO_2-10 nanoparticles was centrifuged at 12,000 rpm for 8 min and washed several times alternately with water and ethanol. The precipitants were then dried at ambient condition and the powder of U-SiO_2-20 and U-SiO_2-10 was collected for further use. S-SiO_2 nanoparticles were prepared via a modified Stöber method. Briefly, 6 mL of TEOS was added to a mixed solution containing 10 mL deionized water, 75 mL ethanol, and 1.6 mL ammonia aqueous under strring. After 8 h stirring, the products were washed by water and ethanol for several times through centrifugation, and then collected after drying at ambient condition. The samples of these silica nanoparticles were then modified with amino groups for subsequent adsorption process. In detail, 50 mg silica samples were dispersed in 30 mL toluene solution which contained 300 μL APTES and refluxed for 8 h at 110 °C. After washing and drying, the products of positively charged silica nanoparticles with amino groups were finally obtained.

2.3 Fabrication of noble metal nanocrystals-decorated silica nanoparticles

AuNCs with a size of ~ 2 nm in diameter were prepared via a THPC reduction process [39]. Firstly, 1.2 mL 80% aqueous THPC solution was diluted to 100 mL with water. Then 1 mL diluted THPC solution was added into a 47 mL aqueous solution containing 3 mL NaOH (0.1 M). After stirring for 2 min, 0.5 mL $HAuCl_4$ (100 mM) was added into the mixture under vigorous stirring and the colour of the solution changed to brown simultaneously, indicating the formation of AuNCs. For the synthesis of Pt nanoparticles, 5 mL of $NaBH_4$ (12 mM) was added dropwise into a mixed solution of 26 mL sodium citrate solution (2.8 mM) and 50 mL of hexachloroplatinic(IV) acid aqueous solution (0.4 mM) under vigorous stirring for 1 h. To prepare the noble metal nanocrystals-decorated silica nanoparticles, 50 mg of silica nanoparticles were added into the fresh prepared noble metal solution and the solution was stirred for 2 h to enable sufficient adsorption. After centrifugation at 12,000 rpm and washing by ethanol, the precipitants of the noble metal-decorated silica nanoparticles were then redispersed in ethanol.

2.4 Preparation of core–shell catalysts of SiO_2@Au@TiO_2

For the preparation of core–shell structure, 50 mg SiO_2@Au, 400 mg HDA, 1 mL $NH_3 \cdot H_2O$, and a pre-setting amount of TIP were sequentially added into 50 mL ethanol for reaction. After stirring for 10 min, the amorphous TiO_2 was coated onto the SiO_2@Au. After repeatedly centrifuged with ethanol and water at 13,000 rpm for 6 min, the precipitate of S-SiO_2@Au@a-TiO_2 was then collected and dried. To obtain the crystalline catalysts SiO_2@Au@TiO_2, the samples were then calcinated at 350 °C. As for the SiO_2-20@Au@TiO_2 for structure characterization, the amount of TIP was set to be 40 μL. As for samples with shell thickness of ~ 20 nm, the TIP was added in four times to avoid aggregation and the total amount of TIP was 140 μL for S-SiO_2@Au@TiO_2, 160 μL for U-SiO_2-10@Au@TiO_2, and 200 μL for U-SiO_2-20@Au@TiO_2, separately. As for U-SiO_2-20@Au@TiO_2 with the shell thickness of 10, 30, and 40 nm, the total TIP amount was 120, 340, and 420 μL, respectively.

2.5 Sample characterization

Transmission electron microscopy (TEM) images were acquired on a JEM-1400 microscope operating at 120 kV. High-resolution TEM (HRTEM) images, high-angle annular dark-field (HAADF) image, and energy-dispersive X-ray spectroscopy (EDXS) mapping were obtained on JEM-2100F microscope (JEOL, Beijing, China) with an accelerating voltage of 200 kV equipped with a post-column Gatan imaging filter. Zeta potential values were measured using a Nano-ZS 90 Nanosizer (Malvern Instruments Ltd., Worcestershire, UK). Extinction spectra were recorded using a Cary 5000 UV–Vis/near infrared ray (NIR) spectrophotometer. The X-ray diffraction (XRD) patterns of different samples were collected by a Bruker D8 powder X-ray diffractometer (Germany) with Ni-filtered Cu Kα radiation (40 kV, 40 mA). The surface areas of the samples were measured with a Micromeritics Tristar 2420 analyzer, ultilizing Brunauer–Emmett–Teller (BET) method for the calculation. The content of gold in SiO_2@Au was determined by an inductively coupled plasma emission spectroscopy instrument (ICP, Thermo Scientific, iCAP 7000 Series).

2.6 Photoelectrochemical properties

Photocurrents were measured in a three-electrode system, in which a Pt wire was used as the count electrode, an Ag/AgCl was used as the reference electrode, and a fluorine-doped tin oxide (FTO) substrate (2 cm × 2 cm) coated with the samples (~ 10 mg) was used as the working electrode. 1.0 M NaOH aqueous solution was used as an electrolyte. A Xe lamp (300 W, Perfectlight Co., Ltd.) with an optical filter (λ > 410 nm) was used as the illumination source. Photocurrent ON/OFF cycles were measured using a CHI660e (CH instruments Co., Ltd.) workstation coupled with a mechanical chopper.

2.7 FDTD calculations

FDTD calculations were used to calculate the local electric field enhancement. In view of the small simulation structures within a few nanometers, total field scattered field (TFSF) source as a special case of plane wave was adopted and to prevent the possible couplings in simulation boundary areas. The specific physical model scale was set according to the TEM results, that is, the diameter of the absorbed AuNCs was 5 nm in smooth silica particle surface and 3.5 nm in spike decorated rough silica particle surface. The size of the spikes of U-SiO_2 was set to be 12 nm at the bottom and 6 nm at the top with a length of 20 nm. In order to reduce the simulation amount, we simply set nine adjacent AuNCs-decorated spikes on silica surface located at the center of the physical domain and neglect the impact of far field. The linearly polarized source was set to propagate along *Z*-axis (top illumination, polarized in-plane) and *Y*-axis (side illumination, polarized out-plane) respectively with a wavelength of 550 nm, thus to clarify the influence of the polarization and direction of the incident beams.

2.8 Degradation of TCH under visible illumination

The reaction solution was prepared by adding 10 mg of photocatalyst into 40 mL of 30 ppm TCH solution. The mixture was stirred in dark for 3 h to reach the adsorption–desorption equilibrium of the photocatalysts for TCH. Then the photocatalytic reaction started by irradiating the mixture with the visible light (λ > 410 nm) using a 300 W Xe arc lamp (λ > 410 nm). 4 mL of sample solutions were taken from the reaction system before the photocatalytic reaction and after the reaction for 30 min. After centrifugation, the optical absorption at 358 nm of the supernatants was recorded with a Varian UV–Vis spectrophotometer (Cary 50, Varian Co.) to calculate the TCH degradation efficiency.

2.9 H_2 generation under solar light illumination

Photocatalytic hydrogen generation was measured using an online photocatalytic hydrogen generation system (Labsolar-6A, Perfectlight Co., Ltd.) at an ambient temperature (25 °C). Fifty milligrams of photocatalysts without co-catalyst was added to an aqueous solution (75 mL of H_2O and 25 mL of methanol) in a closed gas circulation system. Before irradiation, the reactor and the whole gas circulating system were fully degassed to remove air by using a vacuum pump for 30 min. The amount of H_2 generated was determined by gas chromatography (Techcomp 7900, TCD, N_2 carrier). A Xe lamp (300 W, Perfectlight Co., Ltd.) with an optical filter (AM 1.5) was used as the illumination source.

3 Results and discussion

The schematic synthesis process for urchin-like plasmonic photocatalysts consisting of silica nanosupports with a AuNCs interlayer and tunable crystalline TiO_2 shell is illustrated in Fig. 1(a). First, U-SiO_2 with tunable spikes was prepared via a single-micelle epitaxial growth process. Then, AuNCs were uniformly deposited on the surface of the U-SiO_2 through a self-assembly process, and well confined by the matrix, which is the key for stabilizing AuNCs. Subsequently, a tunable TiO_2 layer was coated thereon through a sol–gel coating procedure. At last, the urchin-like photocatalysts (U-SiO_2@Au@TiO_2) were obtained after calcination at 350 °C. For contrast, the crystalline photocatalysts (S-SiO_2@Au@TiO_2) supported with conventional smooth silica nanospheres could be synthesized through the similar process, as shown in Fig. 1(b).

Corresponding to the above fabrication process, the dielectric supports with different surface topological structures were synthesized firstly. The silica nanospheres with smooth surface (S-SiO_2) and diameter of ~ 160 nm were synthesized by classical

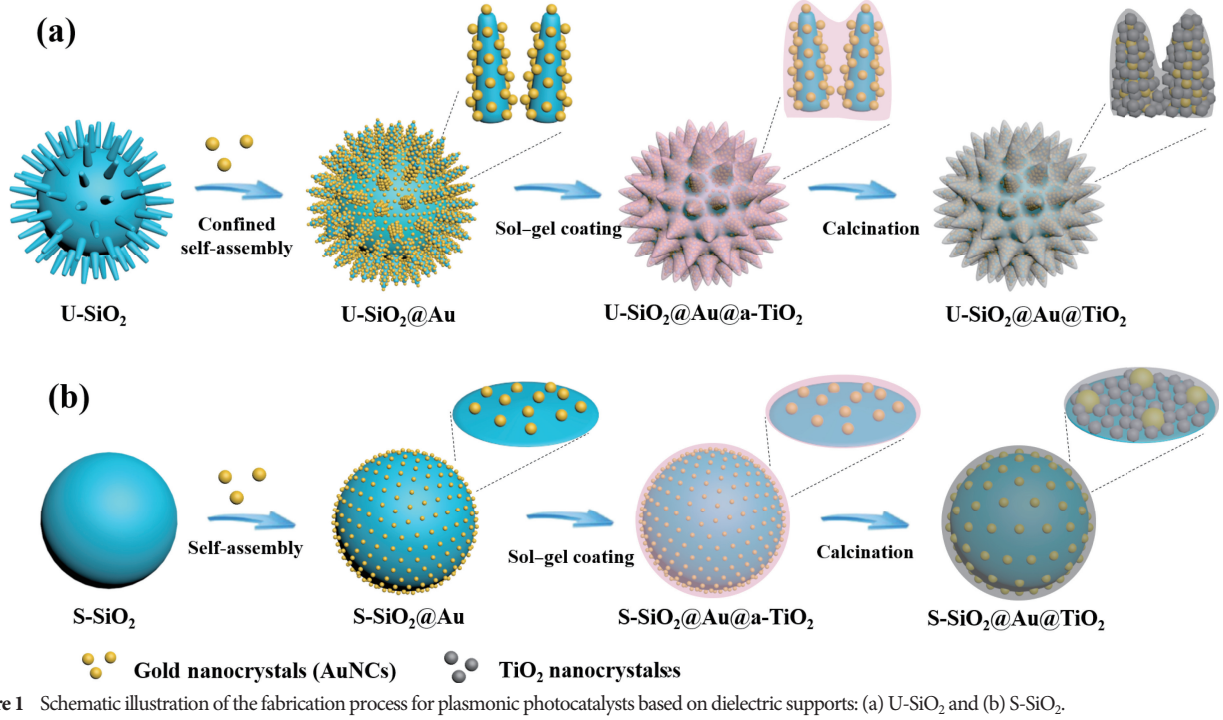

Figure 1 Schematic illustration of the fabrication process for plasmonic photocatalysts based on dielectric supports: (a) U-SiO_2 and (b) S-SiO_2.

Stöber method (Fig. 2(a)). Monodispersed U-SiO_2 with tunable spikes was synthesized in the oil/water biphase system via a single-micelle epitaxial growth process [38]. The TEM images show that the obtained U-SiO_2 with shorter spikes and longer spikes are highly uniform with the diameters of ~ 160 nm (Figs. 2(e) and 2(i)). The length of the spikes can be estimated to be ~ 20 and ~ 10 nm and the samples are denoted as U-SiO_2-20 and U-SiO_2-10. The surface areas of U-SiO_2-20 and U-SiO_2-10 are measured to be ~ 137 and ~ 116 $cm^3 \cdot g^{-1}$, while S-SiO_2 is only ~ 31 $cm^3 \cdot g^{-1}$ in contrast (Fig. S1 in the Electronic Supplementary Material (ESM)). The significantly increased surface area of U-SiO_2 is ascribed to the unique surface topography formed by the tunable spikes. After modifying with amino group on the surface of the above three kinds of silica nanoparticles, the negatively-charged AuNCs with a size of ~ 2 nm (Fig. S2 in the ESM) could be uniformly assembled on the surface of the silica supports via the electrostatic interaction [39], forming AuNCs covered-silica nanocomposites (SiO_2@Au). The variation of the surface zeta potential of all intermediate products was in good agreement with the adsorption process (Fig. S3 in the ESM).

All of the SiO_2@Au samples remain monodisperse (Figs. 2(b), 2(f), and 2(j)). The AuNCs are much more densely and uniformly distributed on U-SiO_2 than that of on S-SiO_2 (Figs. 2(c), 2(g), and 2(k)). According to ICP results (Fig. S4 in the ESM), the Au content of SiO_2-Au in the adsorption saturation state is 8.37% for U-SiO_2-10@Au and 10.38% for U-SiO_2-20@Au, much larger than that of S-SiO_2@Au (which is 4.38%). Almost all the spikes in U-SiO_2 have AuNCs located on the tips (Figs. 2(g) and 2(k)), three examples are highlighted by yellow circles in Fig. 2(k)). More interestingly, the partially enlarged view of U-SiO_2-20@Au (Fig. 2(l)) shows that the AuNCs are prone to adsorb onto sites with high curvatures i.e., the sharp tips of the spikes (the yellow arrows) and the edges of the relatively blunt tips of the spikes (the red arrows). And sufficient adsorption at the tips of the spikes is also observed for Pt nanoparticles (Fig. S5 in the ESM). A series of the adsorption experiments with diluted AuNCs solutions were conducted to explore the above adsorption preference on the spikes of the U-SiO_2. When the concentration of AuNCs solutions was extremely low, the AuNCs only appeared on the tips of the spikes, indicating that AuNCs were preferentially assembled at the tips (Figs. S6(a) and S6(d) in the ESM). As the concentration of the AuNCs increased, more tips were occupied by AuNCs (Figs. S6(b) and S6(e) in the ESM). Further increasing of the concentration of the AuNCs solutions, the whole spikes of the U-SiO_2-20 were covered by AuNCs (Figs. S6(c) and S6(f) in the ESM), leading to a dense distribution on U-SiO_2. The adsorption preference on the tips of the spikes may come from the anisotropic wettability of the U-SiO_2 [40–42]. The tips of the spikes on the surface are more easily wetted than the bottom ends of the spikes, thus the AuNCs in the solution are prone to absorb on the tips of the spikes.

A layer of TiO_2 shell with tunable thickness was sequentially introduced on the surface of SiO_2@Au by sol–gel coating and the amorphous core–shell structures of SiO_2@Au@a-TiO_2 were formed. The TEM images (Fig. S7 in the ESM) show the successful coating of TiO_2 and the SiO_2@Au@a-TiO_2 samples are monodispersed with a uniform size of ~ 180 nm. The XRD patterns (Fig. S8 in the ESM) of these samples show no obvious peaks of crystalline TiO_2, demonstrating the amorphous structure. After annealed at 350 °C, the core–shell structures of SiO_2@Au@TiO_2 were obtained. The SiO_2@Au@TiO_2 samples show good uniformity and dispersity (Figs. 3(a), 3(c), and 3(e)). The AuNCs in S-SiO_2@Au@TiO_2 are distributed unevenly with an

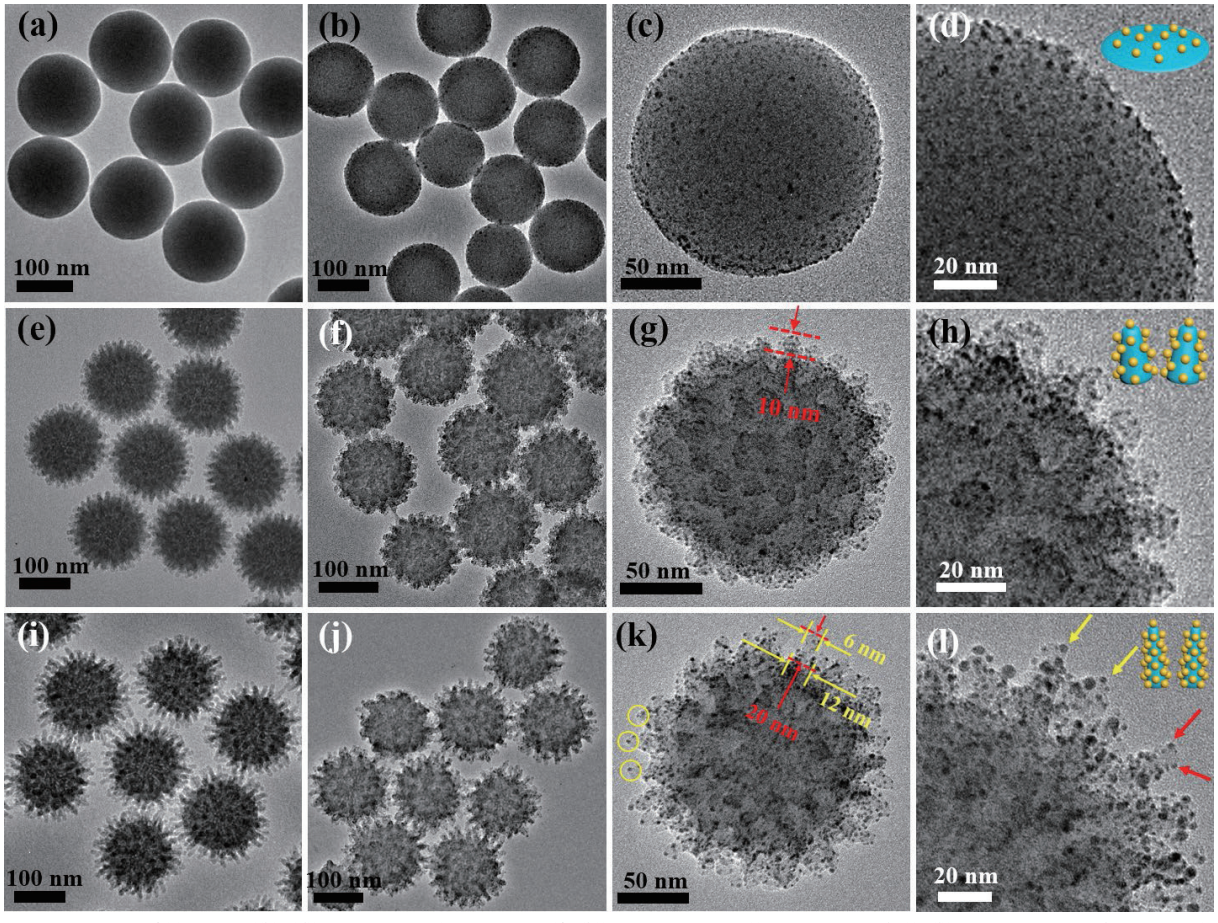

Figure 2 TEM images of (a) S-SiO_2, ((b)–(d)) S-SiO_2@Au, (e) U-SiO_2-10, ((f)–(h)) U-SiO_2-10@Au, (i) U-SiO_2-20, and ((j)–(l)) U-SiO_2-20@Au. The insets in ((d), (h), and (l)) are the schemes of AuNCs on the surfaces of S-SiO_2, U-SiO_2-10, and U-SiO_2-20.

increased size (Fig. 3(b)), indicating a severe aggregation during the crystallization process, which is consistent with previous report of the aggregation of AuNCs in same structure during calcination process [28]. Interestingly, the AuNCs interlayers remain dense and uniform in U-SiO_2@Au@TiO_2 (Figs. 3(d) and 3(f)). The size of the largest gold nanoparticles in U-SiO_2-10@Au@TiO_2 and U-SiO_2-20@Au@TiO_2 is only ~ 4 nm in diameter, while there are aggregates with size increased to ~13 nm in diameter in S-SiO_2@Au@TiO_2, forming a sharp contrast. Further statistical analysis results show that the size distribution of AuNCs in U-SiO_2-10@Au@TiO_2 and U-SiO_2-20@Au@TiO_2 is estimated to be 3.10 ± 0.53 nm (Fig. S9(b) in the ESM) and 3.37 ± 0.58 nm (Fig. S9(c) in the ESM), much smaller and narrower than that of S-SiO_2@Au@TiO_2 (5.35 ± 2.36 nm) (Fig. S9(a) in the ESM). The proportion of AuNCs with a size of < 4 nm is ~ 30.56% in S-SiO_2@Au@TiO_2 (Fig. 3(g)), suggesting the uncontrollable aggregation of AuNCs on S-SiO_2. As for U-SiO_2@Au@TiO_2, the proportion of AuNCs with a size less than 4 nm is ~ 90.38% for U-SiO_2-20@Au@TiO_2 and ~ 92.00% for U-SiO_2-10@Au@TiO_2, indicating that the aggregation is largely suppressed in U-SiO_2@Au@TiO_2.

HRTEM image (Fig. 3(h)) of U-SiO_2-20@Au@TiO_2 shows that the nanoparticles on the surface are crystallized. For the relatively dark nanoparticles, a lattice spacing of 0.20 nm can be observed, being ascribed to the face-centered cubic (fcc) Au (200). While for the relatively light areas, a lattice spacing of 0.32 nm is assigned to tetragonal TiO_2 (101) lattice plane. HAADF and energy-dispersive X-ray (EDX) mapping images of the U-SiO_2-20@Au@TiO_2 (Fig. 3(i)) clearly depict the hierarchical core–shell structures with the urchin-like morphology and the Si, O, Au, and Ti elements are uniformly distributed in this structure. The HAADF and EDX mapping images (Fig. S10 in the ESM) of the U-SiO_2-10@Au@TiO_2 also demonstrate the similar core–shell structure with uniformly distributed AuNCs.

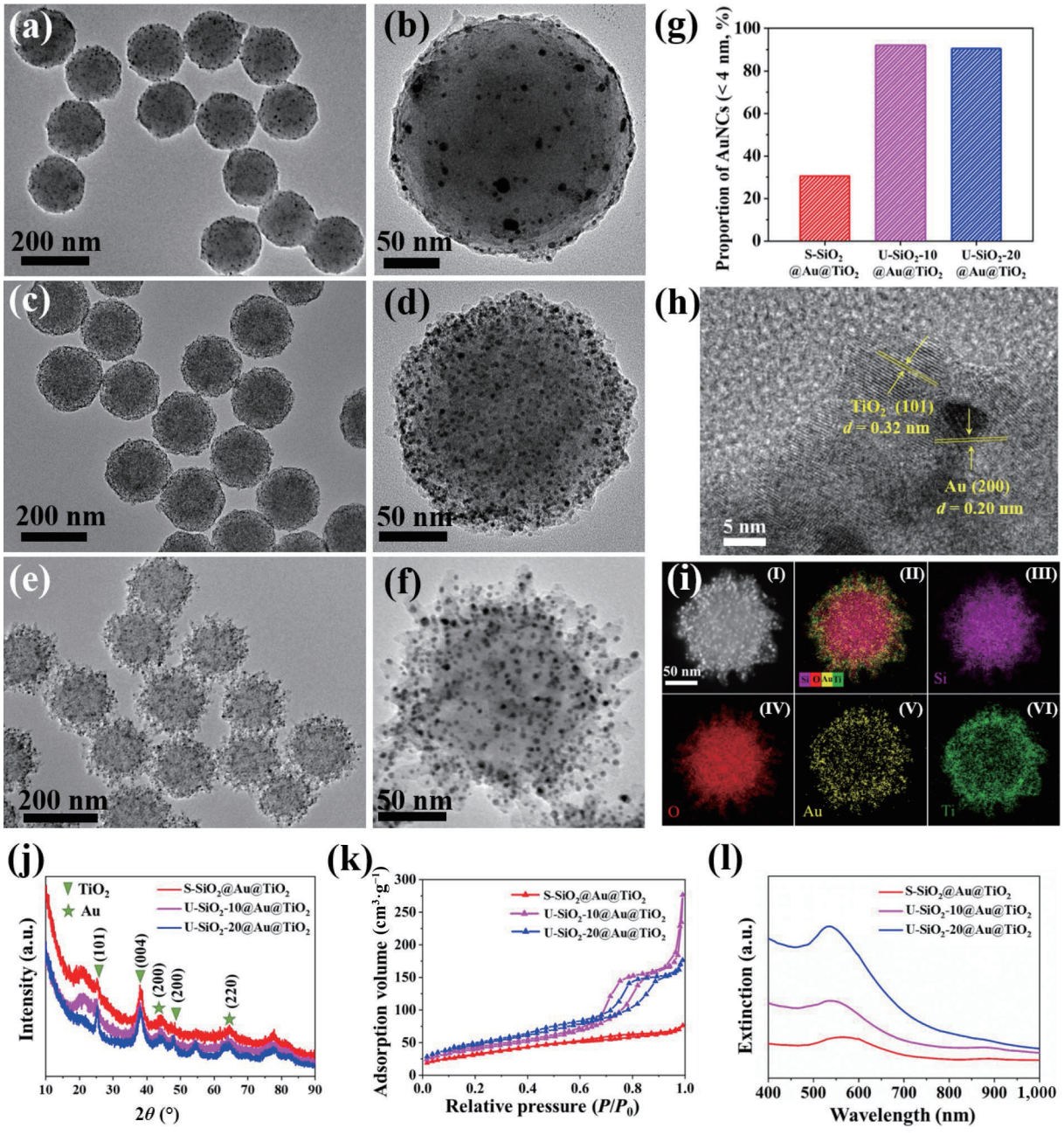

Figure 3 TEM images of ((a) and (b)) S-SiO_2@Au@TiO_2, ((c) and (d)) U-SiO_2-10@Au@TiO_2, and ((e) and (f)) U-SiO_2-20@Au@TiO_2. (g) The proportion of AuNCs with a size less than 4 nm in SiO_2@Au@TiO_2 according to the TEM images in (a)–(f). (h) HRTEM and (i) HAADF and EDX elemental mapping images of U-SiO_2-20@Au@TiO_2. (j) XRD patterns, (k) nitrogen adsorption–desorption isotherms, and (l) DRS of SiO_2@Au@TiO_2 samples.

Since the thickness of TiO_2 shell affects the photocatalytic activity [28, 35], the samples used for comparison were controlled with the same shell thickness of ~ 20 nm (Fig. S11 in the ESM). The XRD patterns of SiO_2@Au@TiO_2 samples with shell thickness of ~ 20 nm are shown in Fig. 3(j). The peaks at 25.3°, 37.9°, and 48.0° correspond to the (101), (004), and (200) crystal planes of anatase TiO_2, respectively (JCPDS no. 21-1272). The wide peaks at 44.4° and 64.6° can be attributed to (200) and (220) crystal planes of Au, respectively (JCPDS no. 04-0784). The surface areas of U-SiO_2-20@Au@TiO_2 and U-SiO_2-10@Au@TiO_2 are calculated to be ~ 171 and ~ 145 $cm^3 \cdot g^{-1}$, respectively, which is much larger than that of S-SiO_2-@Au@TiO_2 (~ 119 $cm^3 \cdot g^{-1}$, Fig. 3(k)). The UV–visible DRS shows that all three samples exhibit SPR absorption at visible light region because of the integrated AuNCs within the structures (Fig. 3(l)), while there was no absorption peak in visible light region for SiO_2@TiO_2 structures with the absence of AuNCs (Fig. S12 in the ESM). The SPR band is located at 535 nm for urchin-like samples of U-SiO_2-20@Au@TiO_2 and U-SiO_2-10@Au@TiO_2 while broadened and red shifted to 570 nm for S-SiO_2@Au@TiO_2, which further confirmed that the distribution of AuNCs in urchin-like samples was much more uniform with a smaller size than that in smooth samples. Moreover, the U-SiO_2-20@Au@TiO_2 exhibits the highest SPR band, indicating the plasmon coupling aroused from the collective excitation of AuNCs in U-SiO_2@Au@TiO_2.

The electric field distributions around the AuNCs-decorated spikes were further simulated by using FDTD calculations. As shown in Figs. 4(a), 4(b), 4(d), and 4(e), the size distribution of AuNCs was tightly assembled on the spikes of the U-SiO_2-20 in U-SiO_2-20@Au@TiO_2 while much more sparsely on the surface of S-SiO_2 in S-SiO_2@Au@TiO_2. Based on the experimental results, the geometric configuration of the model was well established. Briefly, the size of the spikes of U-SiO_2-20 was set to be 12 nm at the bottom and 6 nm at the top with a length of 20 nm while the diameter of AuNCs set to be 3.5 nm in U-SiO_2-20@Au@TiO_2 and 5 nm in S-SiO_2@Au@TiO_2. Excited by the linearly polarized source propagated along *Z*-axis with a wavelength of 550 nm, weak electric field around isolated gold nanoparticles in S-SiO_2@Au (Fig. 4(c)) can be observed. For the U-SiO_2@Au, the plasmonic resonances of adjacent gold nanoparticles strongly coupled, giving rise to plasmon hot spots with highly intense and localized electric field (Fig. 4(f)). Generally, the intensity of SPR increases as the size of gold nanoparticles increases for normal nanostructures with isolated metal particles [43–45]. In this case, the U-SiO_2-20@Au structure with smaller size of gold nanoparticles achieves significantly higher SPR than that of S-SiO_2@Au due to the effective plasmon coupling. Similar phenomenon can be observed when calculating the electric field distributions using the linearly polarized source propagated along *Y*-axis (Fig. S13 in the ESM).

The photocatalytic performance of SiO_2@Au and SiO_2@Au@a-TiO_2 and SiO_2@Au@TiO_2 towards TCH degradation under visible light irradiation (λ > 410 nm) were tested. The adsorption–desorption equilibrium of TCH on the surface of the photocatalysts was achieved in the reaction system before the irradiation and the adsorption amounts of the photocatalysts for TCH were calculated to be 2.30% for S-SiO_2-Au@TiO_2, 2.60% for U-SiO_2-10-Au@TiO_2, and 3.34% for U-SiO_2-20-Au@TiO_2 (Figs. S14 and S15, and Table S1 in the ESM). Under visible light irradiation, the intensity of absorption peak of TCH at the wavelength of 358 nm was rapidly decreased, suggesting the degradation of TCH [46–50]. Notably, the U-SiO_2-20@Au@TiO_2 with plasmon hot spots exhibited the highest enhancement of photocatalytic activity (Fig. 5(a)), achieving 52.91% degradation of TCH after 30 min visible light irradiation, which is a 2.9-fold enhancement comparing to S-SiO_2@Au@TiO_2. The three kinds of photocatalysts of SiO_2@Au@TiO_2 were applied for photocatalytic H_2 generation under solar light. The results show that U-SiO_2-20@Au@TiO_2 obtained the highest H_2 generation rate of 318.35 $\mu mol \cdot h^{-1} \cdot g^{-1}$, U-$SiO_2$-10@Au@$TiO_2$ the medium of 194.13 $\mu mol \cdot h^{-1} \cdot g^{-1}$ while S-SiO_2@Au@TiO_2 the lowest of 82.88 $\mu mol \cdot h^{-1} \cdot g^{-1}$ (Fig. 5(b)). The U-SiO_2-20@Au@TiO_2 with plasmon hot spots contributes to the enhancement of 3.8 times in H_2 generation under solar light in comparison with that of S-SiO_2@Au@TiO_2. These results show that the photocatalysts supported by the urchin-like silica nanoparticles exhibited better photocatalytic performance than that of the conventional smooth nanoparticles. The periodic on/off transient photocurrent response of these samples under the intermittent visible light illumination (λ > 410 nm) shows that the U-SiO_2-20@Au@TiO_2 sample exhibited ~ 3.4-fold enhanced photocurrent density than that of S-SiO_2@Au@TiO_2, indicating that the separation of photo-induced charge carriers over urchin-like photocatalysts had been efficiently facilitated as compared to that of smooth photocatalysts (Fig. 5(c)).

In addition, the photocatalytic activity of H_2 generation significantly increased as the thickness of TiO_2 increased from 10 to 30 nm (Fig. 5(d) and Fig. S16 in the ESM). The H_2

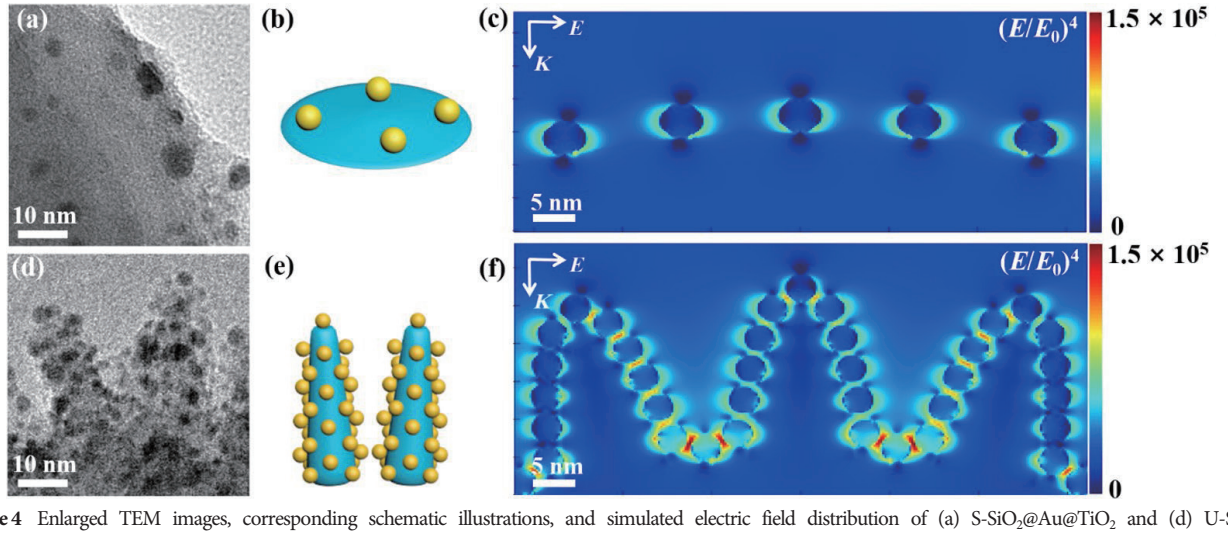

Figure 4 Enlarged TEM images, corresponding schematic illustrations, and simulated electric field distribution of (a) S-SiO_2@Au@TiO_2 and (d) U-SiO_2-20@Au@TiO_2. Schematic illustration of the AuNCs distribution on (b) S-SiO_2@Au in S-SiO_2@Au@TiO_2 and (e) U-SiO_2-20@Au in U-SiO_2-20@Au@TiO_2. Simulated electric field distribution of (c) S-SiO_2@Au and (f) U-SiO_2-20@Au excited by the linearly polarized source propagated along *Z*-axis with a wavelength of 550 nm.

generation rate reached 667.10 μmol·h^{-1}·g^{-1} of U-SiO_2-20@Au@TiO_2 with a TiO_2 thickness of ~ 30 nm, which is 5.2 times higher than that of a TiO_2 thickness of ~ 10 nm. When the shell thickness of TiO_2 was further increased to ~ 40 nm, the H_2 generation rate was only slight improved. A similar trend of varied photocatalytic activity with the thickness of the TiO_2 layer was also observed in TCH degradation (Fig. S17 in the ESM). This may due to that the contact between TiO_2 and AuNCs becomes more sufficient as TiO_2 shell thickness increases from ~10 to ~ 30 nm, while the contact interface of Au-TiO_2 saturates after the shell thickness reaches ~ 30 nm. As shown in Fig. 5(e), it is proposed that TiO_2 nanoparticles tend to aggregate into the gaps between of the spikes on the surface of U-SiO_2-20 during the crystallization process. When the shell thickness was thin, the AuNCs at the tip of the U-SiO_2-20 cannot be fully encapsulated by TiO_2 nanoparticles (Fig. S18(a) in the ESM), resulting in inefficient electron transfer. While thicker coating enabled more sufficient contact between AuNC and TiO_2 (Fig. S18(b) in the ESM), leading to efficient electron transfer. The above experiments together demonstrate that the U-SiO_2 not only ensures a much denser AuNCs distribution which can generate enhanced SPR via plasmon coupling, but also facilitates the sufficient contact between AuNCs and TiO_2, thus enhancing the hot electron generation of AuNCs and the injection into the conduction band of TiO_2 across the Schottky barrier of Au-TiO_2 (Fig. 5(f)). As shown in Fig. 5(g), no apparent activity loss can be observed for H_2 generation during six recycle runs, indicating that U-SiO_2-20@Au@TiO_2 is able to serve as a stable solar light photocatalyst.

4 Conclusions

We demonstrate a space-confined self-assembly strategy for the preparation of urchin-like photocatalyst U-SiO_2@Au@TiO_2 to enhance the SPR effect of sub-5 nm AuNCs by introducing the urchin-like silica nanoparticles with long spikes as the dielectric support. In this case, due to space confinement effect, the U-SiO_2 facilitates the dense and uniform assembly of AuNCs and prevents the aggregation of AuNCs during the crystallization process of TiO_2 layer. In consequence, the dense distribution of AuNCs in U-SiO_2@Au@TiO_2 not only gives rise to highly intense and localized electromagnetic field which was demonstrated by FDTD results, but also enables sufficient contact between AuNCs and TiO_2, forming abundant Schottky junctions for efficient electron transfer. The U-SiO_2-20@Au@TiO_2 contributed to the enhancement of 2.9 times in TCH degradation under visible light illumination and 3.8 times in H_2 generation under solar light in comparison with that of S-SiO_2@Au@TiO_2. We believe our findings in this study create new avenues for tuning the surface plasmon resonance of small metallic nanocrystals for plasmonic-based applications.

Acknowledgements

This work was supported by the National Key Research and Development Program of China (No. 2018YFE0201701), the National Natural Science Foundation of China (Nos. 21975050, 21905052, 11975081, and 22105041), Science and Technology

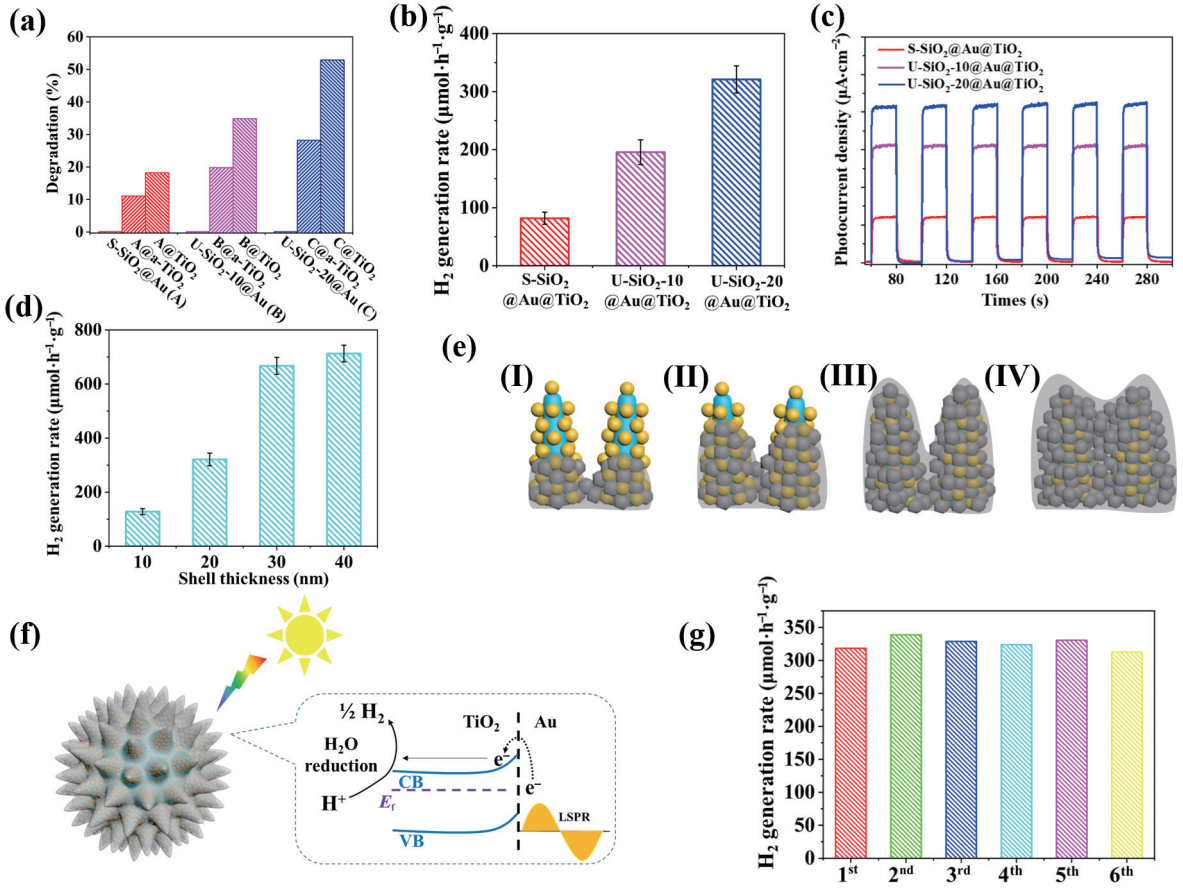

Figure 5 (a) Photocatalytic degradation of TCH under visible illumination (λ > 410 nm) over AuNCs decorated silica supports, amorphous, and crystalline TiO_2 coated photocatalysts. (b) Photocatalytic hydrogen generation under solar light illumination and (c) transient photocurrent densities under visible illumination (λ > 410 nm) over S-SiO_2@Au@TiO_2, U-SiO_2-10@Au@TiO_2, and U-SiO_2-20@Au@TiO_2 with the shell thickness of 20 nm. (d) Photocatalytic hydrogen generation under solar light illumination over U-SiO_2-20@Au@TiO_2 with different TiO_2 shell thickness. (e) Illustration of U-SiO_2-20@Au@TiO_2 samples with different shell thicknesses. (f) Illustration of the proposed photocatalytic enhancement via direct electron transfer in the urchin-like photocatalyst system. (g) Recycling photocatalytic hydrogen generation under solar light illumination over U-SiO_2-20@Au@TiO_2.

Commission of Shanghai Municipality (No. 21ZR1408800), Key Basic Research Program of Science and Technology Commission of Shanghai Municipality (No. 19JC1410700), the Program of Shanghai Academic Research Leader (No. 21XD1420800), and Guangdong Basic and Applied Basic Research Foundation (No. 2021A1515010108).

Electronic Supplementary Material: Supplementary material (further details of the size distribution of AuNCs in various samples, ICP results, TEM images of AuNCs decorated U-SiO_2 with diluted AuNCs solutions, SiO_2@Au@a-TiO_2 structures, XRD patterns, HAADF and EDXS mapping images of SiO_2@Au@TiO_2 samples, DRS results, simulated electric field distribution excited by the linearly polarized source propagated along *Y*-axis, and HAADF images and EDXS linescan profile recorded of the U-SiO_2-20@Au@TiO_2 with the varied shell thicknesses) is available in the online version of this article at https://doi.org/10.1007/s12274-022-4712-9.

References

[1] Liu, D.; Xue, C. Plasmonic coupling architectures for enhanced photocatalysis. *Adv. Mater.* **2021**, *33*, 2005738.

[2] Liu, Y. S.; Deng, J. P.; Jin, Z. C.; Liu, T. X.; Zhou, J.; Luo, F.; Wang, G. F. A study of plasmon-driven catalytic 4-NBT to DMAB in the dry film by using spatial Raman mapping spectroscopy. *Nano Res.* **2022**, *15*, 6062–6066.

[3] Hinman, S. S.; McKeating, K. S.; Cheng, Q. Surface plasmon resonance: Material and interface design for universal accessibility. *Anal. Chem.* **2018**, *90*, 19–39.

[4] Yi, J.; You, E. M.; Ding, S. Y.; Tian, Z. Q. Unveiling the molecule-plasmon interactions in surface-enhanced infrared absorption spectroscopy. *Natl. Sci. Rev.* **2020**, *7*, 1228–1238.

[5] Schuller, J. A.; Barnard, E. S.; Cai, W. S.; Jun, Y. C.; White, J. S.; Brongersma, M. L. Plasmonics for extreme light concentration and manipulation. *Nat. Mater.* **2010**, *9*, 193–204.

[6] Zhan, C.; Liu, B. W.; Huang, Y. F.; Hu, S.; Ren, B.; Moskovits, M.; Tian, Z. Q. Disentangling charge carrier from photothermal effects in plasmonic metal nanostructures. *Nat. Commun.* **2019**, *10*, 2671.

[7] Li, S. S.; Huang, H.; Shao, L.; Wang, J. F. How to utilize excited Plasmon energy efficiently. *ACS Nano* **2021**, *15*, 10759–10768.

[8] Linic, S.; Christopher, P.; Ingram, D. B. Plasmonic-metal nanostructures for efficient conversion of solar to chemical energy. *Nat. Mater.* **2011**, *10*, 911–921.

[9] Kaefer, K.; Krüger, K.; Schlapp, F.; Uzun, H.; Celiksoy, S.; Flietel, B.; Heimann, A.; Schroeder, T.; Kempski, O.; Sönnichsen, C. Implantable sensors based on gold nanoparticles for continuous long-term concentration monitoring in the body. *Nano Lett.* **2021**, *21*, 3325–3330.

[10] Zhan, C.; Chen, X. J.; Yi, J.; Li, J. F.; Wu, D. Y.; Tian, Z. Q. From plasmon-enhanced molecular spectroscopy to plasmon-mediated chemical reactions. *Nat. Rev. Chem.* **2018**, *2*, 216–230.

[11] Ding, S. Y.; You, E. M.; Tian, Z. Q.; Moskovits, M. Electromagnetic theories of surface-enhanced Raman spectroscopy. *Chem. Soc. Rev.* **2017**, *46*, 4042–4076.

[12] Zhang, C. P.; Chen, S.; Jiang, Z. L.; Shi, Z. Y.; Wang, J. L.; Du, L. T. Highly sensitive and reproducible SERS substrates based on ordered micropyramid array and silver nanoparticles. *ACS Appl. Mater. Interfaces* **2021**, *13*, 29222–29229.

[13] Lal, S.; Link, S.; Halas, N. J. Nano-optics from sensing to waveguiding. *Nat. Photon.* **2007**, *1*, 641–648.

[14] Gao, X. X.; Zhang, J. J.; Luo, Y.; Ma, Q.; Bai, G. D.; Zhang, H. C.; Cui, T. J. Reconfigurable parametric amplifications of spoof surface plasmons. *Adv. Sci. (Weinh.)* **2021**, *8*, 2100795.

[15] Shi, K. Z.; Chen, Z. Y.; Xu, X. N.; Evans, J.; He, S. L. Optimized colossal near-field thermal radiation enabled by manipulating coupled Plasmon polariton geometry. *Adv. Mater.* **2021**, *33*, 2106097.

[16] Wang, Z. Y.; Clark, J. K.; Ho, Y. L.; Volz, S.; Daiguji, H.; Delaunay, J. J. Ultranarrow and wavelength-tunable thermal emission in a hybrid metal-optical Tamm state structure. *ACS Photon.* **2020**, *7*, 1569–1576.

[17] Pu, Y. C.; Wang, G. M.; Chang, K. D.; Ling, Y. C.; Lin, Y. K.; Fitzmorris, B. C.; Liu, C. M.; Lu, X. H.; Tong, Y. X.; Zhang, J. Z. et al. Au nanostructure-decorated TiO_2 nanowires exhibiting photoactivity across entire UV–visible region for photoelectrochemical water splitting. *Nano Lett.* **2013**, *13*, 3817–3823.

[18] Ivanchenko, M.; Nooshnab, V.; Myers, A. F.; Large, N.; Evangelista, A. J.; Jing, H. Enhanced dual plasmonic photocatalysis through plasmonic coupling in eccentric noble metal-nonstoichiometric copper chalcogenide hetero-nanostructures. *Nano Res.* **2022**, *15*, 1579–1586.

[19] Laska, M.; Krzemińska, Z.; Kluczyk-Korch, K.; Schaadt, D.; Popko, E.; Jacak, W. A.; Jacak, J. E. Metallization of solar cells, exciton channel of plasmon photovoltaic effect in perovskite cells. *Nano Energy* **2020**, *75*, 104751.

[20] Bao, Z. Y.; Fu, N. Q.; Qin, Y. Q.; Lv, J.; Wang, Y.; He, J. J.; Hou, Y. D.; Jiao, C. Y.; Chen, D. C.; Wu, Y. C. et al. Broadband plasmonic enhancement of high-efficiency dye-sensitized solar cells by incorporating Au@Ag@SiO_2 core–shell nanocuboids. *ACS Appl. Mater. Interfaces* **2020**, *12*, 538–545.

[21] Atta, S.; Pennington, A. M.; Celik, F. E.; Fabris, L. TiO_2 on gold nanostars enhances photocatalytic water reduction in the near-infrared regime. *Chem* **2018**, *4*, 2140–2153.

[22] Huang, X. Q.; Li, Y. J.; Chen, Y.; Zhou, H. L.; Duan, X. F.; Huang, Y. Plasmonic and catalytic AuPd nanowheels for the efficient conversion of light into chemical energy. *Angew. Chem., Int. Ed.* **2013**, *52*, 6063–6067.

[23] Yu, G. Y.; Qian, J.; Zhang, P.; Zhang, B.; Zhang, W. X.; Yan, W. F.; Liu, G. Collective excitation of plasmon-coupled Au-nanochain boosts photocatalytic hydrogen evolution of semiconductor. *Nat. Commun.* **2019**, *10*, 4912.

[24] Ma, J. M.; Liu, X. F.; Wang, R. W.; Zhang, F.; Tu, G. L. Plasmon-induced near-field and resonance energy transfer enhancement of photodegradation activity by Au wrapped CuS dual-chain. *Nano Res.* **2022**, *15*, 5671–5677.

[25] Kumar, A.; Kumari, N.; Dubbu, S.; Kumar, S.; Kwon, T.; Koo, J. H.; Lim, J.; Kim, I.; Cho, Y. K.; Rho, J. et al. Nanocatalosomes as plasmonic bilayer shells with interlayer catalytic nanospaces for solar-light-induced reactions. *Angew. Chem., Int. Ed.* **2020**, *59*, 9460–9469.

[26] Burda, C.; Chen, X. B.; Narayanan, R.; El-Sayed M, A. Chemistry and properties of nanocrystals of different shapes. *Chem. Rev.* **2005**, *105*, 1025–1102.

[27] Tsukamoto, D.; Shiraishi, Y.; Sugano, Y.; Ichikawa, S.; Tanaka, S.; Hirai, T. Gold nanoparticles located at the interface of anatase/rutile TiO_2 particles as active plasmonic photocatalysts for aerobic oxidation. *J. Am. Chem. Soc.* **2012**, *134*, 6309–6315.

[28] Weng, B.; Lu, K. Q.; Tang, Z. C.; Chen, H. M.; Xu, Y. J. Stabilizing ultrasmall Au clusters for enhanced photoredox catalysis. *Nat. Commun.* **2018**, *9*, 1543.

[29] Zhang, N.; Han, C.; Xu, Y. J.; Foley IV, J. J.; Zhang, D. T.; Codrington, J.; Gray, S. K.; Sun, Y. G. Near-field dielectric scattering promotes optical absorption by platinum nanoparticles. *Nat. Photon.* **2016**, *10*, 473–482.

[30] Naya, S. I.; Niwa, T.; Kume, T.; Tada, H. Visible-light-induced electron transport from small to large nanoparticles in bimodal gold nanoparticle-loaded titanium(IV) oxide. *Angew. Chem., Int. Ed.* **2014**, *53*, 7305–7309.

[31] Qian, H. F.; Zhu, M. Z.; Wu, Z. K.; Jin, R. C. Quantum sized gold nanoclusters with atomic precision. *Acc. Chem. Res.* **2012**, *45*, 1470–1479.

[32] Dutta, S. K.; Mehetor, S. K.; Pradhan, N. Metal semiconductor heterostructures for photocatalytic conversion of light energy. *J. Phys. Chem. Lett.* **2015**, *6*, 936–944.

[33] Lee, J. H.; Shin, Y.; Lee, W.; Whang, K.; Kim, D.; Lee, L. P.; Choi, J. W.; Kang, T. General and programmable synthesis of hybrid liposome/metal nanoparticles. *Sci. Adv.* **2016**, *2*, 1601838.

[34] Kelly, K. L.; Coronado, E.; Zhao, L. L.; Schatz, G. C. The optical properties of metal nanoparticles: The influence of size, shape, and dielectric environment. *J. Phys. Chem. B* **2003**, *107*, 668–677.
[35] Han, C.; Li, S. H.; Tang, Z. R.; Xu, Y. J. Tunable plasmonic core–shell heterostructure design for broadband light driven catalysis. *Chem. Sci.* **2018**, *9*, 8914–8922.
[36] Zhang, Y. L.; Zhang, J. Y.; Zhang, B. S.; Si, R.; Han, B.; Hong, F.; Niu, Y. M.; Sun, L.; Li, L.; Qiao, B. T. et al. Boosting the catalysis of gold by O_2 activation at Au-SiO_2 interface. *Nat. Commun.* **2020**, *11*, 558.
[37] Koo, W. T.; Kim, Y.; Savagatrup, S.; Yoon, B.; Jeon, I.; Choi, S. J.; Kim, I. D.; Swager, T. M. Porous ion exchange polymer matrix for ultrasmall Au nanoparticle-decorated carbon nanotube chemiresistors. *Chem. Mater.* **2019**, *31*, 5413–5420.
[38] Wang, W. X.; Wang, P. Y.; Tang, X. T.; Elzatahry, A. A.; Wang, S. W.; Al-Dahyan, D.; Zhao, M. Y.; Yao, C.; Hung, C. T.; Zhu, X. H. et al. Facile synthesis of uniform virus-like mesoporous silica nanoparticles for enhanced cellular internalization. *ACS Cent. Sci.* **2017**, *3*, 839–846.
[39] Duff, D. G.; Baiker, A.; Edwards, P. P. A new hydrosol of gold clusters. 1. Formation and particle size variation. *Langmuir* **1993**, *9*, 2301–2309.
[40] Bahng, J. H.; Yeom, B.; Wang, Y. C.; Tung, S. O.; Hoff, J. D.; Kotov, N. Anomalous dispersions of "hedgehog" particles. *Nature* **2015**, *517*, 596–599.
[41] Wang, S. T.; Liu, K. S.; Yao, X.; Jiang, L. Bioinspired surfaces with superwettability: New insight on theory, design, and applications. *Chem. Rev.* **2015**, *115*, 8230–8293.
[42] Liu, W. D.; Liu, X. Y.; Xiang, S. Y.; Chen, Y. X.; Fang, L. P.; Yang, B. Functional interface based on silicon artificial chamfer nanocylinder arrays (CNCAs) with underwater superoleophobicity and anisotropic properties. *Nano Res.* **2016**, *9*, 3141–3151.
[43] Yu, Y.; Xie, Y. J.; Zeng, P.; Zhang, D.; Liang, R. Q.; Wang, W. X.; Ou, Q. R.; Zhang, S. Y. Morphology-tailored gold nanoraspberries based on seed-mediated space-confined self-assembly. *Nanomaterials (Basel)* **2019**, *9*, 1202.
[44] Liu, X.; Yang, Y.; Mao, L. G.; Li, Z. J.; Zhou, C. J.; Liu, X. H.; Zheng, S.; Hu, Y. X. SPR quantitative analysis of direct detection of atrazine traces on Au-nanoparticles: Nanoparticles size effect. *Sensor. Actuat. B Chem.* **2015**, *218*, 1–7.
[45] Qian, K.; Sweeny, B. C.; Johnston-Peck, A. C.; Niu, W. X.; Graham, J. O.; DuChene, J. S.; Qiu, J. J.; Wang, Y. C.; Engelhard, M. H.; Su, D. et al. Surface plasmon-driven water reduction: Gold nanoparticle size matters. *J. Am. Chem. Soc.* **2014**, *136*, 9842–9845.
[46] Wu, S. Q.; Hu, H. Y.; Lin, Y.; Zhang, J. L.; Hu, Y. H. Visible light photocatalytic degradation of tetracycline over TiO_2. *Chem. Eng. J.* **2020**, *382*, 122842.
[47] Li, C. M.; Yu, S. Y.; Che, H. N.; Zhang, X. X.; Han, J.; Mao, Y. L.; Wang, Y.; Liu, C. B.; Dong, H. J. Fabrication of Z-scheme heterojunction by anchoring mesoporous γ-Fe_2O_3 nanospheres on g-C_3N_4 for degrading tetracycline hydrochloride in water. *ACS Sustainable Chem. Eng.* **2018**, *6*, 16437–16447.
[48] Wang, X. N.; Jia, J. P.; Wang, Y. L. Combination of photocatalysis with hydrodynamic cavitation for degradation of tetracycline. *Chem. Eng. J.* **2017**, *315*, 274–282.
[49] Ji, B.; Zhang, J. X.; Zhang, C.; Li, N.; Zhao, T. T.; Chen, F.; Hu, L. H.; Zhang, S. D.; Wang, Z. Y. Vertically aligned ZnO@ZnS nanorod chip with improved photocatalytic activity for antibiotics degradation. *ACS Appl. Nano Mater.* **2018**, *1*, 793–799.
[50] Wu, Z. J.; Guo, K.; Cao, S.; Yao, W. Q.; Piao, L. Y. Synergetic catalysis enhancement between H_2O_2 and TiO_2 with single-electron-trapped oxygen vacancy. *Nano Res.* **2020**, *13*, 551–556.